Multiple Cascade Radiation Damage Simulations of Pyrochlore

A. Archer,[a] H. R. Foxhall,[b] N. L. Allan,[a] J. R. W Shearer,[a] D. S. D. Gunn[c] J. H. Harding,[b] I. T. Todorov,[c] K. P. Travis,[b] and J. A. Purton[c]

We report molecular dynamics simulations of multiple radiation damage cascades in the pyrochlores $Gd_2Ti_2O_7$ and $Gd_2Zr_2O_7$ and in the solid solution $Gd_2(Zr_xTi_{1-x})_2O_7$ (x = 0.25, 0.50, 0.75). Using a simulation cell of approximately 360,000 atoms, for each compound 2,200 decay events are simulated over a total time of 10 ns, with each recoiling uranium atom (primary knock on atom, PKA) being assigned an initial kinetic energy of 5 keV. The structures generated in the simulations are analysed using Steinhardt local order parameters. There is a large increase in volume for the Ti pyrochlore associated with a transition to an amorphous structure which resembles the melt while preserving the immediate local environment of the Ti. The calculated dose for amorphisation is approximately 20 eV atom^{-1} which compares well with experiment[1]. It appears to be the overlap of cascade and damage accumulation that drives the amorphisation and eventually suppresses the healing mechanisms. We have examined the variation in amorphous fraction with the number of decay events – an expression with two rather than one exponential terms reproduces the simulation data well. The behaviour of the zirconate is quite different – the substantial anion disorder produced by each recoil event is followed by healing between cascade events and reversion to the parent pyrochlore. In the solid solution the onset of amorphisation is delayed to successively later times on increasing the Zr concentration and the overall swelling reduced. Our simulations highlight the importance of ion mobility, associated with the weaker Zr-O bonds, in the healing process.

Introduction

The search for materials not subject to structural failure after prolonged radiation damage is of considerable interest, societal as well as scientific[2-4]. Yet our understanding of radiation damage at the atomistic level remains incomplete. Crystalline pyrochlores are potential hosts for plutonium from the decommissioning of atomic weapons and spent fuel-reprocessing operations. Accordingly in this paper we examine radiation damage in the series $Gd_2(Zr_xTi_{1-x})_2O_7$, ($0 \le x \le 1$), since this shows a dramatic variation in the extent of damage with composition.

From the results of heavy ion bombardment experiments Wang et al.[5], predicted that an increase in Zr leads to dramatic increase in radiation tolerance, with lifetimes lengthened from a thousand to over a million years[6]. A radiation-induced crystalline-amorphous transition in $Gd_2Ti_2O_7$ produces a metamict state[5,7]. In contrast, $Gd_2Zr_2O_7$ under the same conditions is transformed to defect fluorite, which is a crystalline structure related to the pyrochlore but with the cations distributed at random. $Gd_2Ti_2O_7$ is thus one of the titanate pyrochlores most susceptible to ion irradiation-induced amorphisation. This calls into question the selection of SYNROC C related titanate phases, betafite $(Ca,U)Ti_2O_7$[8] and zirconolite $CaZrTi_2O_7$[9] as principal candidates for Pu-immobilization despite their apparent longevity in geological environments, where they are found as metamict phases. $Gd_2Ti_2O_7$ is thus a useful model system because of the attention it has received both experimentally[10–13] and theoretically[6,14–22] and its close similarity to the SYNROC C related titanate phases. The explanation for such different behaviour of two pyrochlores as closely related as $Gd_2Ti_2O_7$ and $Gd_2Zr_2O_7$ must ultimately lie at the atomic level and this remains the subject of much attention and conjecture[23].

Upon emission of an alpha particle, the radioactive isotope releases an α-particle and recoils in the opposite direction, with a kinetic energy of thousands of electron volts. The recoiling heavy actinide atom is conventionally referred to as a Primary Knock on Atom (PKA), and as it moves through the lattice it generates substantial disorder. The degree of disorder varies from system to system, as does the degree of subsequent healing. (e.g. refs. 14, 15, 23–30). One powerful atomistic technique is molecular dynamics (MD) (e.g. Chartier et al.,[29] Devanathan[20], Trachenko et al.[32], Purton et al.[6,16,22], Foxhall et al.[30], Aidhy et al[33]). Due to the large energy of the PKAs very large simulation cells are required, even reaching the order of several million atoms. Such large cascade simulations approach the limits of feasibility given available computational resources. Virtually all studies of ceramics have thus been restricted to single cascades for reasons of computational expense. Yet by themselves most single cascades are followed by extensive healing and almost complete recovery to the parent compound. This paper in contrast is devoted to multiple cascade simulations in $Gd_2(Zr_xTi_{1-x})_2O_7$ in order to explore the cascade-overlap processes, which often eventually lead to amorphisation, and probe their consequences. Our simulations therefore include multiple overlap events at short time intervals. Somewhat surprisingly there has been little such work involving multiple cascade simulations in the literature; the only such studies of which we were aware are simulations in SiC[4], UO_2[54] and metals alloys[55-57]. However, these involved fewer overlapping cascades at lower energies than the ones presented in this study.

The pyrochlore (PYR) structure (space group Fd3m), is similar to fluorite and is shown in Figure 1. Cations with formal +3 (Gd) and +4 charge (Ti, Zr) occupy 16d and 16c sites respectively. Oxide ions at the 48f site have two +3, two +4 nearest cation neighbours, while anions at 8b are surrounded by four +3 cations. The vacant 8a site has four +4 cation neighbours. +3 cations are eightfold coordinate to oxygen while +4 are sixfold coordinate. At high temperature, in $Gd_2Zr_2O_7$ the 8a site is partially occupied and there is intrinsic anion disorder associated with high ionic conductivity;[35] this is not observed in $Gd_2Ti_2O_7$ indicating much lower oxygen mobility in the Ti compound.

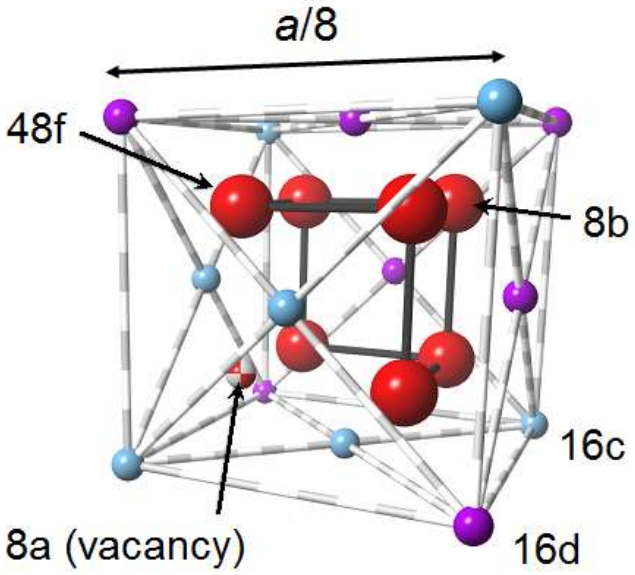

Figure 1 One-eighth of the unit cell of the pyrochlore (PYR) $Gd_2M_2O_7$ (M=Ti,Zr) structure. Gd^{3+} ions are purple, Ti/Zr^{4+} ions are blue and O^{2-} ions are red. The anion vacancy is also shown in red/white.

The defect fluorite (DF) structure is similar to pyrochlore but with a random distribution of Gd and Ti/Zr over the cation sites and also random distribution of oxygen over the 8a and 8b sites. Since the light oxide ions have a much higher mobility than Gd, Ti and Zr, we also consider an anion-disordered pyrochlore form (ADP) in which just the oxygen sublattice is disordered over 8a and 8b, but cation ordering is retained. There is also the possibility of forming zones in which a region of one phase is surrounded by another i.e., a nucleation centre has formed. So it is also useful to define explicitly an intermediate structure (INT) structure which is 20% DF in which the cubic DF "core" is surrounded by pure pyrochlore (PYR) and a further structure DF/AM which contains both DF and amorphous (AM).

Radiation Damage Cascades

Molecular Damage Simulations

This paper is principally concerned with the difference in radiation tolerance of Gd pyrochlores with varying Ti and Zr content as measured using simulations involving multiple cascades. The setup of the molecular dynamics simulations is broadly similar to those of the single cascade events reported previously[6,36]. We used the DL_POLY 4 code[37], cubic simulation cells containing 360,448 atoms, and a set of new interatomic potentials recently suggested by Gunn et al.[18]. In the mixed Ti/Zr systems cation positions were assigned at random to Ti or Zr; a recent configurational averaging[38] study of the solid solution has concluded from the calculated enthalpies of mixing (~ 0 kJ mol^{-1}) that the solution is almost ideal[39]. The length of the simulation cell was the appropriate multiple (16) of the experimental lattice parameter, the initial temperature set to 300 K and equilibration (before any of the damage events) was performed for 10 ps in the NPT-ensemble with a timestep of 2 fs, and a pressure of 1 atm. All cascade simulations used the NPT ensemble with 360 U^{3+} ions replacing Gd^{3+} ions as the PKAs. For each cascade a U^{3+} ion was randomly selected and projected in a random direction by assigning to it an excess kinetic energy equivalent to the chosen recoil energy, here set to 5 keV. A variable timestep was used for the cascade simulations to ensure that during the early steps of each cascade, the timestep was sufficiently short to allow for the presence of fast moving, highly energetic atoms, while maintaining overall resource efficiency for subsequent stages. The simulations used the Langevin barostat (2 ps^{-1}) and the Nosé-Hoover thermostat with a 31.8 fs relaxation time. In all there were 2,200 alpha decay events in each of the simulations, each separated by 5 ps, following the suggestions of Trachenko et al.[40] who discuss typical recovery times in ceramics. The total length of the simulation for each of the compositions ($Gd_2(Ti_xZr_{1-x})_2O_7$, x=0.00, 0.25, 0.50, 0.75, 1.00) was close to 10 ns. It is worth noting that the thermostat relaxation time was selected so that the model system was adequately thermalised between consecutive cascades at reasonable compute cost. Given the model system size and size and rate of energy insertion a smaller relaxation time would over-heal the system and underestimate damage severely whereas a larger one would lead to system overheat and subsequent melting due to our choice of energy and frequency of PKA insertion. We verified that single cascade damage size and morphology under these conditions were in agreement with those for the same energy cascade carried out in much larger model systems with larger relaxation times for both the barostat and thermostat.

Steinhardt order parameters

To analyse the simulations we make extensive use of Steinhardt order analysis, as adapted for radiation damage problems by Archer et al.[36]. Local bond-order or Steinhardt order parameters41 are often used to distinguish between crystalline structures and polytopes[42]. The parameters are translationally and rotationally invariant. Each of the atoms is selected in turn from the simulation cell. For each vector *r* which connects atom *i* to those within a given cut-off distance (the primary cut-off), a set of even-order spherical harmonics[43] Q_{lm} are calculated:

$$Q_{lm}(\mathbf{r}) = Y_{lm}(\theta(\mathbf{r}),\phi(\mathbf{r})) \quad (1)$$

where ϑ and φ are the polar angles defining the orientation of *r*. The average value of Q_{lm} over the N_b neighbours within the cut-off distance is:

$$Q_{lm}(i) = \frac{1}{N_b(i)} \sum_{j=1}^{N_b(i)} Q_{lm}(j) \qquad (2)$$

To obtain a rotationally invariant quantity we now average over all possible values of *m* for a given *l* to obtain the order parameter $Q_l(i)$:

$$Q_l(i) = \sqrt{\frac{4\pi}{2l+1} \sum_{m=-1}^{l} |Q_{lm}(i)|^2} \qquad (3)$$

We calculate a further average of $Q_l(i)$ over all the atoms *i* in spherical regions of radius 12 Å (the secondary cut-off distance) each centred on one of the atoms in the simulation cell, finally obtaining a value of Q_l for each region. We refer to such regions as secondary spheres. We can in principle also average just the Q_l for all regions centred on a particular atom type (Gd,Ti/Zr,O) to obtain Q_l(Gd), Q_l(Ti/Zr) and Q_l(O). We use primary and secondary cut off distances set to 3.2 Å and 12 Å respectively, as in our previous study[36]. The primary distance is such that just nearest neighbours are included in calculation of the individual Q_{lm}.

Before considering the complex situations accompanying radiation damage one must construct signatures for each structure to be used in the subsequent assignment and so we start with a consideration of the Steinhardt parameters for equilibrium $Gd_2(Ti/Zr)_2O_7$ structures. Figures 2a-e show, for example, the order parameter Q2 evaluated for the series $Gd_2(Ti_xZr_{1-x})_2O_7$ (where x=0.00, 0.25, 0.50, 0.75, 1.00) for the PYR, ADP and DF structures, and for the pure Ti compound, the two-phase structure INT as discussed in the introduction. ADP is unstable and cannot be equilibrated for the pure titanate itself. We have found it sufficient to work only with Q_2, Q_4 and Q_{10}, as together they provide sufficient information to assign a structural type to any region of material. Each plot in Figure 3 displays the distribution of order parameters over the course of a dynamics run of 10 ns for a particular system with a simulation cell of 360,448 atoms.

We next require a method of assigning a structural type to a secondary sphere in the damaged system given a set of values of the parameter Q_l for different *l*. There is of course no unique procedure for this. When the order parameters all lie in a region where there is only one Q_l curve from the different possibilities, the choice is trivial. If, though, a calculated index lies in a region where several Q_l curves overlap, it could apply to multiple structures and then we assign it to the strongest structural signal. For example, a Q_4 value of 0.34 for $Gd_2Zr_2O_7$ in Fig. 3b is classified as ADP. A structural type can only be assigned to a region if at least two of the three indices for a particular secondary sphere give the same result. Otherwise the region is assigned a label of "amorphous/other", which for simplicity we abbreviate to "amorphous". For values lying outside the regions corresponding to any of the five structures (i.e., outside the limits on the x-axes in Figures 2a-e) then the "amorphous" label is also applied.

One further step and check is needed; we need to check that the apparent Q_l value for the secondary sphere region is not simply an artefact produced by averaging the individual $Q_l(i)$ signals corresponding to two different structures.

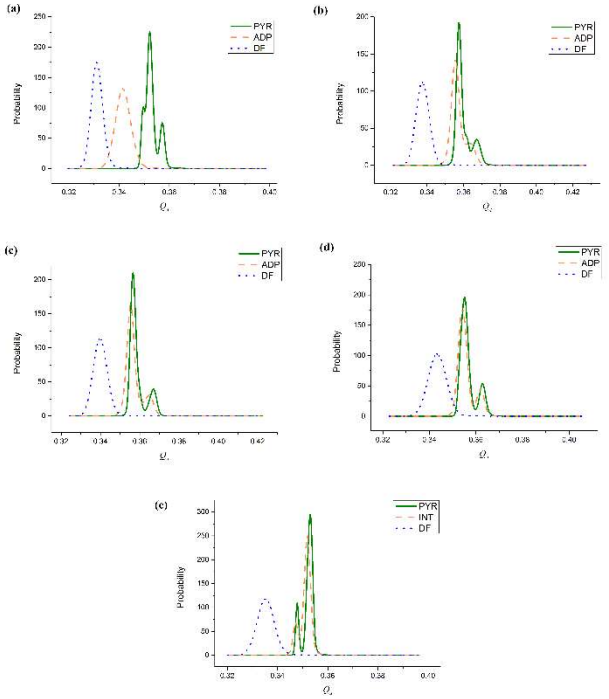

Figure 2 Steinhardt order parameter (Q_4) probability distributions (probability density functions) for the series of compounds $Gd_2(Ti_xZr_{1-x})_2O_7$. Values of x are as follows: a) 0.00, b) 0.25, c) 0.50, d) 0.75 and e) 1.00. The structural types PYR, ADP and DF are considered for compounds a-d, while for compound e the two-phase structure (INT) as described in the text, is also displayed. ADP cannot be isolated for the pure titanate. Each curve is normalised so that the area under each curve is one.

To illustrate the problem, the histograms in Figure 3 show the distributions of unaveraged Steinhardt parameters $Q_4(i)$ for a secondary sphere, one before (Figure 3a) and the second after (Figure 3b) the onset of amorphisation in a radiation damage simulation of $Gd_2Zr_2O_7$. The procedure in the previous paragraph classifies this region as "pyrochlore" in both cases. However, if we examine the $Q_4(i)$ more closely we see that such a classification is misleading after amorphisation takes place. It is clear that the order parameters after amorphisation take a much wider range of values, although the mean remains similar, and it is this which is responsible for a misleading classification of Figure 3(b) as PYR if we look only at the mean of the values in the histogram.

In Figure 3(b) the $Q_4(i)$ values have a much wider spread and range over values corresponding to the defect fluorite (DF) and amorphous (AM) structures. The parameters for DF and AM lie either side of the PYR probability distribution; averaging over a secondary sphere containing these two structures causes the region to be classified as PYR. The parameter signature in Figure 3(b) is typically found between amorphous and DF regions. Thus we also monitor the standard deviation of the unaveraged order parameters $Q_4(i)$ for each of the cations and when this is larger than 0.001 then the region is labelled as DF/AM.

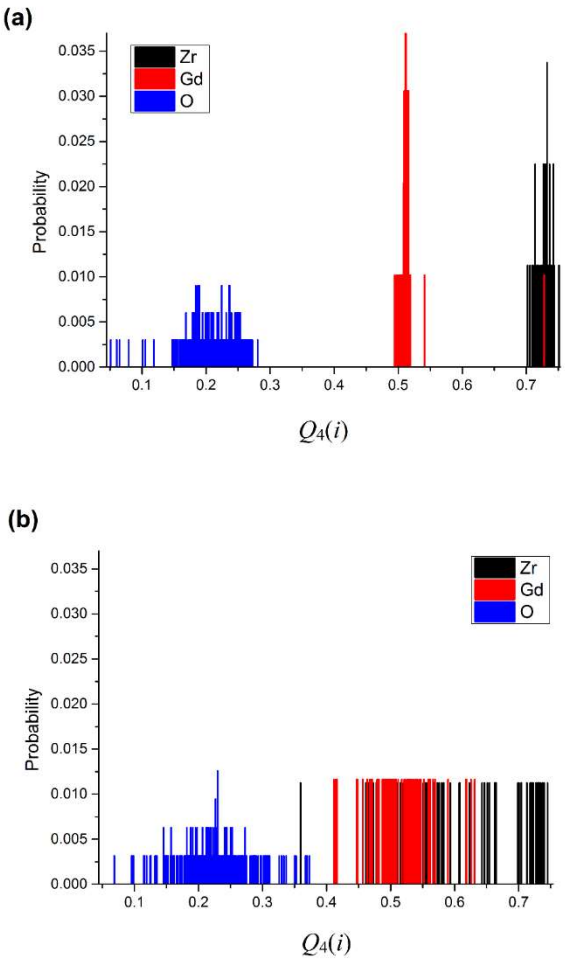

Figure 3 Histograms showing the unaveraged Steinhardt order parameters $Q_4(i)$; i = Zr, Gd, O for two apparent "pyrochlore" secondary spheres in a radiation damage simulation of $Gd_2Zr_2O_7$. The colour coding denotes the atom at the centre of the primary sphere. Figure 3(a) and 3(b) shows the parameters before and after the onset of amorphisation respectively. Figure 3(a) is classified PYR, the classification of the second is discussed in the text.

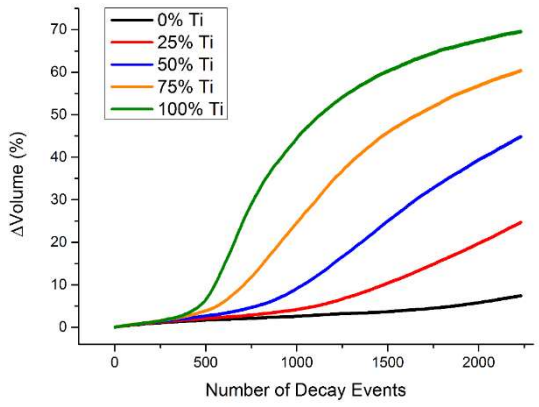

Figure 4 The percentage change in volume during the multiple cascade simulation as a function of Ti content.

Results and Discussion

Volumes

We start with monitoring the overall changes to the volume of the simulation cells. Figure 4 shows the percentage volume change during the course of the simulation for the end-members and the solid solutions. There are dramatic variations with Zr content. Whereas after 10 ps the volume of $Gd_2Zr_2O_7$ has increased only by 10%, that of $Gd_2Ti_2O_7$ has increased by 70%, consistent with amorphisation in the latter but little change in the former. Because of the much larger rate of energy input into the cell compared with experimental ion irradiation it is problematic to compare this value with experiment[44–46]. Increasing the Ti content leads to successively larger volume changes. At a given time the increase in volume does not vary linearly with Ti content, with the largest increase between 25% Ti and 50% Ti. We return to consider the kinetics of the volume change in a subsequent section.

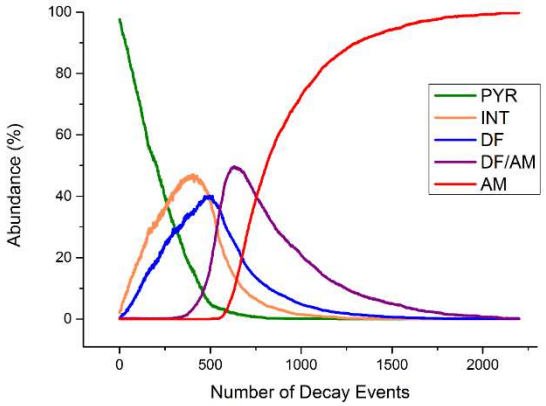

Figure 5 The relative abundances of pyrochlore (PYR), the PYR/DF intermediate (INT), defect fluorite (DF), defect fluorite/amorphous (DF/AM) and amorphous (AM) structures in $Gd_2Ti_2O_7$ as a function of time determined by Steinhardt order parameter analysis.

Structures

Results obtained using the modified Steinhardt parameters Ql to determine the relative abundance of the different structural types throughout the multiple cascade simulations for the end-member $Gd_2Ti_2O_7$ are shown in Figure 5. The simulation begins with an accumulation of anion and cation disorder which peaks at around 400 decay events. Shortly after, there is a rapid increase in the amount of regions identified as the DF/AM structure type as the amorphisation of the system begins. The cascades begin to produce amorphous clusters large enough to dominate regions of the simulation cell after 500 decay events, signified by the appearance of AM regions. The simulation cell is fully amorphised after around 1,750 simulated alpha decay events (approximately 8.15 ns). Notice that the amorphisation process occurs over the same period of time as the rapid increase in volume observable in Figure 2. The radial distribution functions of the AM were compared to those of PYR and the AM, unlike PYR, has no medium or long-range order.

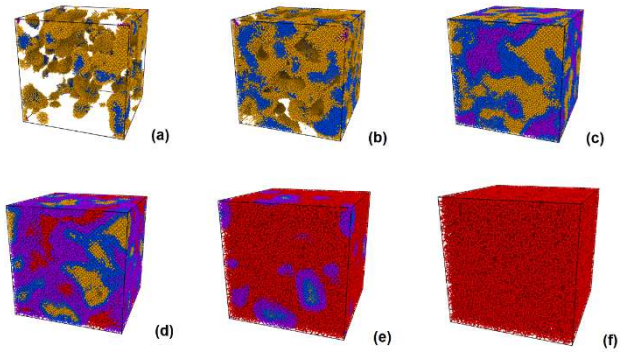

Figure 6 Analysis of selected frames of the simulation in $Gd_2Ti_2O_7$ after a) 65, b) 252, c) 500, d) 625, e) 1000 and f) 2,200 decay events. Each orange sphere represents a spherical region with a radius of 12 Å in which the dominant structure is INT as indicated by the Q_l values. Blue denotes defective fluorite and red denotes amorphous. Regions that are pyrochlore are not shown.

Figure 6 shows the entire cell and those regions where the averaged Q_l indicates a local INT (PYR/DF, orange), DF (blue) or amorphous (red) region during the course of the simulation. Pyrochlore regions are not shown for clarity. Image 6(a) shows the damage formed by the initial cascades, some of which overlap to form disordered networks. Notice how the cascade tracks have DF cores surrounded by a halo of partially damaged regions (INT). This feature is consistent with the ion bombardment studies of Lang et al.[11–13]. Figure 6(b) shows the growth of this disorder network while images (c) and (d) show a dramatic increase in the number of DF/AM (and in 6(d), AM) regions which indicates the start of the collapse of the system to amorphous. In $Gd_2Ti_2O_7$ this is a rapid process once started and although the snapshot detailed in image 6(e) is only 375 decay events later, the amorphisation has advanced radically, leaving only small nanodomains of crystalline regions. Finally, image (f) shows the system after 2,200 decay events and at this point it is fully amorphous (RDF confirmed). The calculated dose for amorphisation (90% amorphous state at 1500 PKAs) is ~20 eV atom^{-1}, which compares well with experiment[3].

For the analogous simulation with 75% Ti, 15% ADP is produced straight away and as shown in Figure 7 the simulation begins similarly to that of the Ti pyrochlore, with a rapid increase in anion and cation disorder. The increase is not as sudden as in $Gd_2Ti_2O_7$ itself, and the total crystalline disorder (ADP+DF) has a maximum value about 10% less. The amorphisation process begins after around 300 decay events with a sharp increase of DF/AM before larger clusters of amorphous regions form. The simulation cell reaches 95% AM after 2,200 decay events.

After 167 decay events (Figure 8(a)) the simulation cell is marbled with ADP and DF. The amount of DF then increases (Figure 8(b)) before being replaced (Figure 8(c)) by DF/AM signalling the beginning of the amorphisation process. After 1,260 decay events, the majority of the simulation cell is amorphous, interrupted by a few veins of heavily disordered crystalline regions. By the end of the simulation only 5% of the predominantly amorphous cell is crystalline.

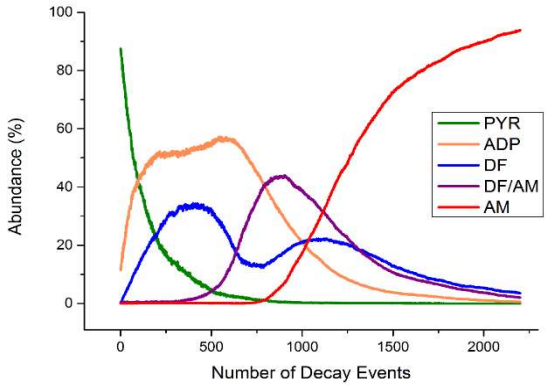

Figure 7 The relative abundance of pyrochlore (PYR), anion disordered pyrochlore (ADP), defect fluorite (DF), defect fluorite/amorphous interface (DF/AM), amorphous (AM) and unknown crystalline structures in $Gd_2Ti_{1.5}Zr_{0.5}O_7$ as a function of time as determined by Steinhardt order parameter analysis.

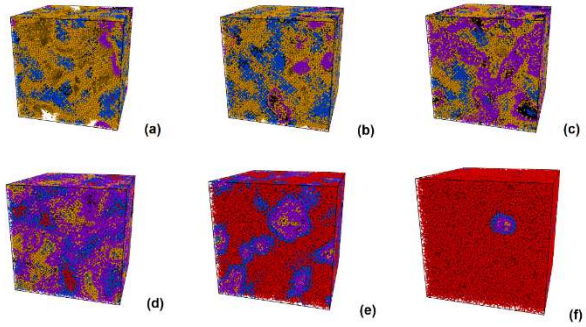

Figure 8 Analysis of selected frames of the simulation in $Gd_2Ti_{1.5}Zr_{0.5}O_7$ after a) 167, b) 489, c) 679, d) 865, e) 1260 and f) 2,200 decay events. Each orange sphere represents a spherical region with a radius of 12 Å in which the dominant structure is ADP as indicated by the Q_l values. Blue denotes defective fluorite and red denotes amorphous. Regions that are pyrochlore are not shown.

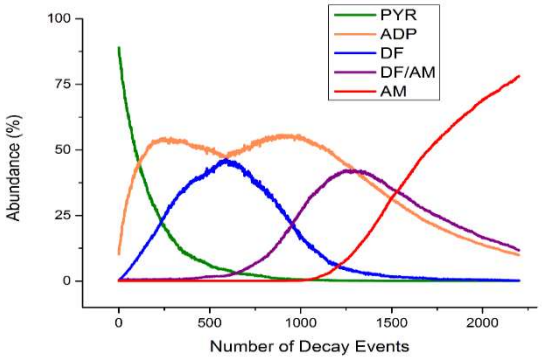

Figure 9 The relative abundance of pyrochlore (PYR), anion disordered pyrochlore (ADP), defect fluorite (DF), defect fluorite/amorphous (DF/AM), amorphous (AM) and unknown crystalline structures in Gd_2TiZrO_7 as a function of time determined by Steinhardt order parameter analysis.

For the 50:50 composition, as with the previous simulations, the first hundred decay events cause a rapid increase in the ADP abundance, although the growth of the DF structure lags slightly behind the ADP in this case (Figure 9). The amount of DF at its peak is greater than in the other simulations which most likely arises due to the increased Zr content and therefore greater stability of the DF structure. The amorphisation process also begins later with increased Zr content at around 500 decay events, shown by the increase in DF/AM regions. The amorphous clusters increase in size after 1,200 decay events forming AM regions and by the end of the simulation the cell reaches a peak of 78% amorphisation.

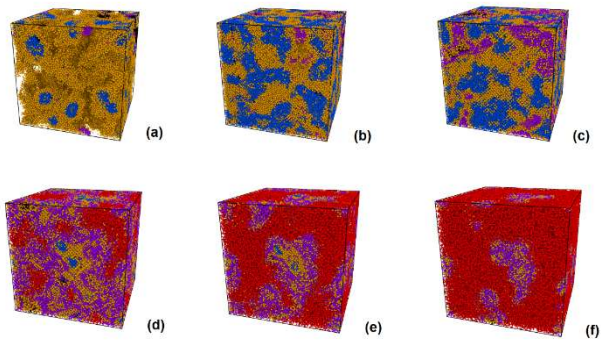

Figure 10 Analysis of selected frames of the simulation in Gd_2TiZrO_7 after a) 95, b) 500, c) 860, d) 1327, e) 1699 and f) 2,200 decay events. Each orange sphere represents a spherical region with a radius of 12 Å in which the dominant structure is ADP as indicated by the Q_l values. Blue denotes defective fluorite and red denotes amorphous. Regions that are pyrochlore are not shown.

Figure 10 shows that in the simulation of the 50:50 solid solution multiple partially overlapping cascade tracks form first, as in the previous cases. After 500 decay events (Figure 10(b)) many of the cascade tracks have combined and most parts of the cell exhibit some level of anion or cation disorder while remaining crystalline. The amount of DF decreases at around 860 decay events (Figure 10(c)) as it is replaced by DF/AM and by 1,327 events (Figure 10(d)) the cascades begin to generate AM regions. This process occurs more slowly than in the compounds with higher Ti content. By 2,200 decay events (Figure 10(f)) the cell is mostly amorphous (78%) except for a small amount of crystalline patches.

For 75% Zr, as shown in Figure 11, the simulations begin with an accumulation of ADP and DF structural types as the cascades progress. Again the peaks are broader than previously for lower Zr content. The transient structure types (ADP and DF) are more easily tolerated and have longer lifetimes. Amorphisation begins at around 1,000 decay events signified by a large increase in the amount of DF/AM regions in the cell. By the end of the simulation the cell is around 20% amorphous, a considerable decrease on the 50% Zr result.

In the 75% Zr system, after 64 decay events (Figure 12a) the damage mostly involves anion disorder and so ADP is the dominant structural type.

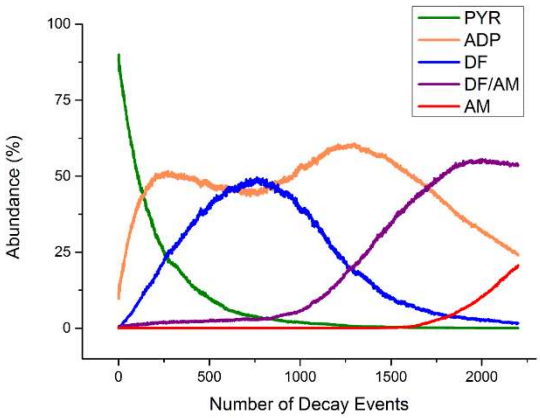

Figure 11 The relative abundance of pyrochlore (PYR), anion disordered pyrochlore (ADP), defect fluorite (DF), defect fluorite/amorphous (DF/AM), amorphous (AM) and unknown crystalline structures in $Gd_2Ti_{0.5}Zr_{1.5}O_7$ as a function of time determined by Steinhardt order parameter analysis.

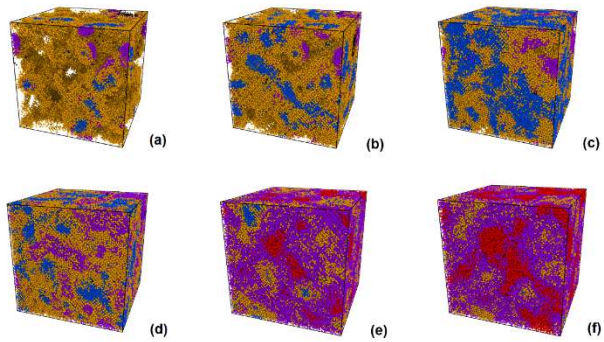

Figure 12 Analysis of selected frames of the simulation in $Gd_2Ti_{0.5}Zr_{1.5}O_7$ after a) 64, b) 250, c) 730, d) 1234, e) 1946 and f) 2,200 decay events. Each orange sphere represents a spherical region with a radius of 12 Å in which the dominant structure is ADP as indicated by the Q_l values. Blue denotes defective fluorite and red denotes amorphous. Regions that are pyrochlore are not shown.

The snapshots at 250 and 730 decay events highlight an increase in defect fluorite implying that cation antisite defects are beginning to cluster (Figure 12(b) and (c)). ADP peaks around 1,234 decay events as the system begins to amorphise, shown by the increased amount of DF/AM regions (Figure 12d). The crystalline cell begins to develop veins of amorphous regions (Figure 12e) as well as a further increase in the DF/AM structure type.

ADP in the pure zirconate is formed more readily, as well as DF, due to the high oxygen mobility in this end-member. In this this study the zirconate end member shows different behaviour, since the energy input, due to the large number of decay events, is sufficient to melt the entire simulation cell as the calculation proceeds, unlike any of the other systems discussed above. The zirconate experimentally has the lowest melting point (the Zr-O bond is weaker than the Ti-O) and with our choice of PKA energy the melt down is a viable outcome. Monitoring of the root

mean square displacements of the cations with time confirms this phase change, as vibrations around lattice sites change into displacements which vary linear with time. Melting begins at around 2000 decay events, coinciding with an increase in volume. There is no metamictisation for this compound which is consistent with ion bombardment experiments[11–13]. Our thesis is that for smaller energy injections per PKA, when kinetic energy dissipation is sufficient to keep the sample temperature sufficiently below its melting point in multiple cascade events, the DF and ADP phases would reach steady state equilibrium, with the PYR phase disappearing. This is consistent with the increased stability of the zirconate relative to that of the pure titanate system, which is prone to amorphisation as observed experimentally. Indeed, the delay in the onset of the AF (red curves in Figures 5, 7, 9 and 11) with dosage clearly demonstrates the increased resistance to amorphisation with increasing of Zr fraction in the simulated systems, which also supports experiment. It is also worth noting that our results show that damage on the oxygen sublattice occurs prior to that on the cation sublattice, as indicated by the first peak of the ADP (orange) curves in Figures 5 (INT), 7, 9 and 11. The position of the well between the double peak in the orange curves, present only in the pyrochlore systems containing Zr, correlates well with the position of the DF-phase peak. With time, the DF fraction decreases as some DF reverts to ADP, leading to the second ADP peak, while the rest becomes more disordered and the DF/AM fraction increases. This is also an early indication of AM seeding prior to eventual melting. The delay of onset with dosage of these changes supports increasing resistance to amorphisation with increasing Zr composition. This behaviour also suggests that in a situation avoiding melting the ADP and DF fractions would reach a steady state with increasing time. The observed amorphisation of $Gd_2Zr_2O_7$ could be an artefact of the differences between simulation and experimental set-ups. Experimentally, a full sample amorphisation and melt-down is avoided as irradiation is only focused on part of the target while the rest of it serves as a thermal bath. Also, the experimental target is not a perfect crystal, and defects and impurities could also act as heat sinks.

Kinetics of Swelling

We have analysed empirically the damage kinetics of the 5 keV multiple decay event simulations by fitting a number of equations to the amorphous fraction of the simulation cell, f_a, as determined by the modified Steinhardt order parameters. Weber et al.[47] have collected together a number of possible irradiation induced amorphisation models. Of these, the functional forms of the Direct Impact, Cascade Overlap and the Direct Impact/Cascade Overlap models all yield very poor fits and so we not consider these further here. Due to this poor performance, we have also tried fit the amorphous fraction variation to expressions suggested by the Direct Impact/Defect Stimulated (DI/DS) and Nucleation and Growth (N&G) models. The direct impact/defect stimulated model takes the form:

$$f_a = 1 - \frac{(A+S)}{\{S + A\exp[(A+S)D]\}}, \qquad (4)$$

where D is the dose and σ_a and σ_s are fitting parameters (formally the amorphisation volume and the stimulated amorphisation volume, respectively)[48]. In our fits we take D as the total number of decay events per simulation cell at time t. In contrast the nucleation and growth model (equation (5)),

$$f_a = 1 - \exp\left[-RG^{m-1}\left(\frac{D}{\varphi}\right)^m\right], \qquad (5)$$

is based on the use of a modified Avrami equation[49] to describe the nucleation and growth of amorphous clusters and we take R, G, m and φ as fitting parameters. The parameter R reflects the nucleation rate of amorphous clusters. The parameter G is related to the growth rate of amorphous clusters and the parameter m the reaction order.

The results of these attempts to fit our simulation data for $Gd_2Ti_2O_7$ to equations of the form of (4) and (5) are shown in Figure 13. Results for all the compositions of the solid solution are similar so are not reproduced here.

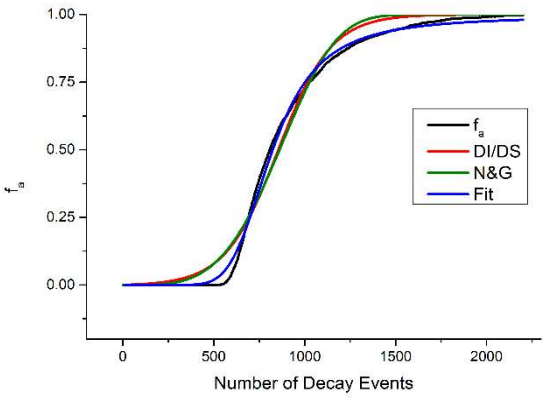

Figure 13 The variation in amorphous fraction (f_a) of the simulation cell in a multiple decay event simulation in $Gd_2Ti_2O_7$. For the fit to equation 6, A = 0.025, B = 4712, C = 0.027, E = 4756 per simulation cell.

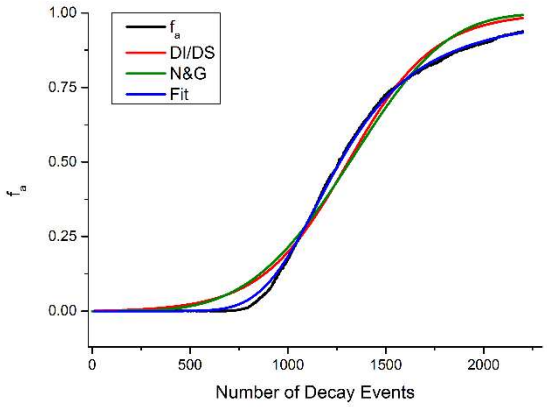

Figure 14 The variation in amorphous fraction (f_a) of the simulation cell in a multiple decay event simulation in $Gd_2Ti_{1.5}Zr_{0.5}O_7$. In the fit to equation 6, A = 0.105, B = 5872, C = 0.107, E = 5723 per simulation cell.

It is clear from the Figure that neither equation (4) or (5) produce satisfactory fits. In particular, the asymmetry is not reproduced; healing is much more efficient when the number of decay events is small. We have found purely empirically that a much more satisfactory fit that can take account of this asymmetry is to a function of the form:

$$f_a = \frac{1}{1 - A\ exp(B/D) + C\ exp(E/D)} \qquad (6)$$

where *A*, *B*. *C* and *E* are parameters determined by fitting, and D the dose, again taken to equal the number of decay events (in the simulation cell). The two exponential terms in the denominator in equation (6) could possibly relate to two different processes such as healing, and damage respectively. The resulting fits are much more successful. Figure 14 shows that the same conclusion applies to $Gd_2Ti_{1.5}Zr_{0.5}O_7$, where the healing is more pronounced.

Conclusions

We have carried out molecular dynamics simulations of two thousand radiation damage cascades over approximately 10 ns in the pyrochlores $Gd_2Ti_2O_7$ and $Gd_2Zr_2O_7$ and in the solid solution $Gd_2(Zr_xTi_{1-x})_2O_7$. The simulations were analysed using local order parameters. There is a large increase in volume for the Ti pyrochlore associated with a transition to an amorphous form. As the Zr content increases, the amorphisation is delayed, a difference associated with enhanced oxygen mobility and the weaker Zr-O bond. The overall swelling over the timescale of the simulation is reduced. Our calculated dose for amorphisation in the Ti end member, which is fully amorphous after roughly 1500 cascades, compares well with experiment. We have examined the variation in amorphous fraction with the number of decay events and suggested that an expression of the form of equation (6) provides a good fit.

Such behaviour is consistent with ion bombardment experiments[11,12,13] and has been suggested previously either indirectly on the basis of calculated static defect energies[19,25,50,51] or inferred from simulations of just one cascade,[6,14,16,20–22,36,52] which however by themselves lead to very little retention of any damage. It appears to be the overlap of cascade and damage accumulation that drives the amorphisation and eventually suppresses the healing mechanisms. Our simulations highlight the importance of ion mobility in the healing process.

It will be interesting in future work to compare the results here with those using longer time-scale methods to simulate the fate of the host material, such as adaptive kinetic Monte Carlo.[53] Simulations of the type reported here should be widely applicable to other materials and also start to provide more quantitative information as to the long-term degradation under radiation damage. Comparison of defect processes in the bulk with those at interfaces will also be worthwhile not only for possibly discovering different defect-lead atomic level mechanisms and processes at such interfaces but also for predicting the behaviour of the host glass matrix surrounding the crystalline ceramic.

Acknowledgements

Support from EPSRC is gratefully acknowledged (grants EP/H013814/1, EP/H012230/1 and EP/H012990/1). AA thanks EPSRC for a project studentship. All the cascade runs were carried out using the computational facilities of the Advanced Computing Research Centre, University of Bristol – http://www.bris.ac.uk/acrc/.

Notes and references

1 Lian, J. et al., *Nucl. Instrum. Methods Phys. Res. Sect. B-Beam Interact. Mater. At.*, 2006, **250**, 128.

2 Lumpkin, G. R., *Elements*, 2006, **2**, 365.

3 Omel'yanenko, B. I., Petrov, V. A. & Poluektov, V. V., *Geol. Ore Depos.*, 2007, **49**, 378. The experimental dosage of the order of 10^{19} α-particles (with energy of ~10 keV per α-particle) per gram of $Gd_2Ti_2O_7$ (mass of 522 gram mol^{-1}) translates to an amorphisation dose of 0.5×10^{26} eV per mol of $Gd_2Ti_2O_7$. The simulation dosage for amorphisation of $Gd_2Ti_2O_7$ is calculated as the product of the PKA energy by the number of events leading to 90% amorphisation, divided by the total number of atoms in the MD cell. This results in 20 eV per atom or 1.4×10^{26} eV per mol of $Gd_2Ti_2O_7$.

4 Ringwood, A. E., Kesson, S. E., Ware, N. G., Hibberson, W. & Major, A., *Nature*, 1979, **278**, 219.

5 Wang, S. X. et al., *J. Mater. Res.*, 1999, **14**, 4470.

6 Todorov, I. T., Purton, J. A., Allan, N. L. & Dove, M. T., *J. Phys.-Condens. Matter*, 2006, **18**, 2217.

7 Lian, J., Wang, L. M., Haire, R. G., Helean, K. B. & Ewing, R. C., *Nucl. Instrum. Methods Phys. Res. Sect. B-Beam Interact. Mater. At.*, 2004, **218**, 236.

8 Mazzi, F. & Munno, R., *Am. Mineral.*, 1983, **68**, 262.

9 Rossell, H. J., *Nature*, 1980, **283**, 282.

10 Wang, J., Lang, M., Ewing, R. C. & Becker, U., *J. Phys.-Condens. Matter*, 2013, **25**, 135001.

11 Lang, M. et al., *Phys. Rev. B*, 2009, **79**, 9.

12 Lang, M. et al., *J. Mater. Res.*, 2009, **24**, 1322.

13 Lang, M. et al., *Nucl. Instrum. Methods Phys. Res. Sect. B Beam Interact. Mater. At.*, 2014, **336**, 102.

14 Chartier, A., Catillon, G. & Crocombette, J. P., *Phys. Rev. Lett.*, 2009, **102**, 4.

15 Wang, X. J., Xiao, H. Y., Zu, X. T., Zhang, Y. & Weber, W. J., *J. Mater. Chem. C*, 2013, **1**, 1665.

16 Purton, J. A. & Allan, N. L., *J. Mater. Chem.*, 2002, **12**, 2923–2926.

17 Catillon, G. & Chartier, A., *J. Appl. Phys.*, 2014, **116**, 193502.

18 Gunn, D. S. D. et al., *J. Mater. Chem.*, 2012, **22**, 4675.

19 Whittle, K. R. et al., *30th Symposium on Scientific Basis for Nuclear Waste Management*, 2006, **985**, 329.

20 Devanathan, R. & Weber, W. J., *J. Appl. Phys.*, 2005, **98**, 086110.

21 Devanathan, R., Weber, W. J. & Gale, J. D., *Energy Environ. Sci.*, 2010, **3**, 1551.

22 Todorov, I. T., Allan, N. L., Purton, J. A., Dove, M. T. & Smith, W., *J. Mater. Sci.*, 2007, **42**, 1920.

23 Ewing, R. C., *Mineral. Mag.*, 2011, **75**, 2359.

24 Devanathan, R., Weber, W. J. & Gale, J. D., *Energy Environ. Sci.*, 2010, **3**, 1551.

25 Sattonnay, G. & Tetot, R., *J. Phys.-Condens. Matter A*, 2014, **26**, 315007.

26 Chartier, A., Van Brutzel, L. & Crocombette, J.-P., *Nucl. Instrum. Methods Phys. Res. Sect. B Beam Interact. Mater. At.*, 2012, **286**, 154.

27 Moll, S. et al., *Phys. Rev. B*, 2011, **84**, 11.

28 Chartier, A., Meis, C., Crocombette, J. P., Weber, W. J. & Corrales, L. R., *Phys. Rev. Lett.*, 2005, **94**, 4.

29 Davoisne, C. et al. in Advances in Materials Science for Environmental and Nuclear Technology (eds. Fox, K., Hoffman, E., Navinnjooran & Pickrell, G.) 3–9 (John Wiley & Sons, Inc., 2010)
30 Foxhall, H. R., Travis, K. P., Hobbs, L. W., Rich, S. C. & Owens, S. L., *Philos. Mag*., 2013, **93**, 328.
31 Mulroue, J., Morris, A. J. & Duffy, D. M., *Phys. Rev. B*, 2011, **84**, 094118.
32 Trachenko, K. et al., *Nucl. Instrum. Methods Phys. Res. Sect. B Beam Interact. Mater. At*., 2012, **277**, 6.
33 Aidhy, D. S. et al., *Sci. Rep*., 2015, **5**, 16297.
34 Gao, F. & Weber, W. J., *J. Mater. Res*., 2002, **17**, 259.
35 Tuller, H. L., J. Phys. Chem. Solids, 1994, **55**, 1393.
36 Archer, A. et al., *J. Phys. Condens. Matter*, 2014, **26**, 485011.
37 Todorov, I. T., Smith, W., Trachenko, K. & Dove, M. T., *J. Mater. Chem*., 2006, **16**, 1911.
38 Allan, N. L. et al., *Phys. Rev. B*, 2001, **63**, 094203.
39 Shearer J., Archer A. & Allan N. L. (unpublished results).
40 Trachenko, K., Dove, M., Artacho, E., Todorov, I. & Smith, W., *Phys. Rev. B*, 2006, **73**, 174207.
41 Steinhardt, P. J., Nelson, D. R. & Ronchetti, *Phys. Rev. B*, 1983, **28**, 784.
42 Moroni, D., ten Wolde, P. R. & Bolhuis, P. G., *Phys. Rev. Lett*., 2005, **94**, 235703.
43 Morse, P. M. & Feshbach, H. Methods of theoretical physics. (McGraw-Hill, 1953).
44 Li, Y. H. et al., *Nucl. Instrum. Methods Phys. Res. Sect. B-Beam Interact. Mater. At*., 2012, **287**, 130.
45 Strachan, D. M. et al., *J. Nucl. Mater*., 2005, **345**, 109.
46 Weber, W. J., Hess, N. J. & Maupin, G. D., *Nucl. Instrum. Methods Phys. Res. Sect. B Beam Interact. Mater. At.*, 1992, **65**, 102.
47 Weber, W. J., *Nucl. Instrum. Methods Phys. Res. Sect. B Beam Interact. Mater. At*., 2000, **166**, 98.
48 Hecking, N., Heidemann, K. F. & Te Kaat, E., *Nucl. Instrum. Methods Phys. Res. Sect. B Beam Interact. Mater. At*., 1986, **15**, 760.
49 Avrami, M., J. Chem. Phys., 1941, 9, 177.
50 Jiang, C., Stanek, C. R., Sickafus, K. E. & Uberuaga, B. P., *Phys. Rev. B*, 2009, **79**, 5.
51 Minervini, L., Grimes, R. W., Tabira, Y., Withers, R. L. & Sickafus, K. E., *Philos. Mag. -Phys. Condens. Matter Struct. Defects Mech. Prop*., 2002, **82**, 123.
52 Ewing, R. C., Weber, W. J. & Lian, J., *J. Appl. Phys*., 2004, **95**, 5949.
53 Gunn, D. S. D., Allan, N. L. & Purton, J. A., *J. Mater. Chem. A*, 2014, **2**, 13407.
54 Martin G., Garcia P., Sabathier C., Devynck F., Krack M., & Maillard S., *Nuclear Instruments and Methods in Physics Research Section B*, 2014, **327**, 108.
55 Gao, F., Bacon D.J., Calder A.F., Flewitt P.E.J., & Lewis T.A., *J. Nucl. Mater.*, 1996, **230**(1), 47.
56 Spaczer M., Caro A., Victoria M., & Diaz de la Rubia T., *Nuclear Instruments and Methods in Physics Research B*, 1995, **102**, 81.
57 Levo, E., Granberg, F., Fridlund, C., Nordlund, K., & Djurabekova, F., *Journal of Nuclear Materials*, 2017, **490**, 323.